Journal of Advanced Ceramics
2023, **12**(8): 1547–1561
https://doi.org/10.26599/JAC.2023.9220771
ISSN 2226-4108
CN 10-1154/TQ

Research Article

Ultrasensitive room-temperature geranyl acetone detection based on Fe@WO_{3-x} nanoparticles in cooked rice flavor analysis

Zichen Zheng[a], Kewei Liu[a], Yiwen Zhou[a], Marc Debliquy[b], Chao Zhang[a,*]

[a]*College of Mechanical Engineering, Yangzhou University, Yangzhou 225127, China*
[b]*Service de Science des Matériaux, Faculté Polytechnique, Université de Mons, Mons 7000, Belgium*

Received: March 23, 2023; Revised: May 8, 2023; Accepted: May 23, 2023
© The Author(s) 2023

Abstract: In the assessment of food quality, geranyl acetone plays a crucial role as a volatile organic compound (VOC) biomarker for diverse agricultural products, while the ultralow concentration detection meeting application requirements has been barely studied. Herein, an iron (Fe)-doped WO_{3-x} gas sensor was employed for greatly sensitive, selective, and scalable geranyl acetone detection. The results proved that precisely-regulated oxygen vacancy (O_V) and sophisticatedly-active electron transition of Fe-doped WO_{3-x} nanoparticles were fulfilled by modifying the doping amount of Fe^{3+}, leading to the prominently enhanced sensitivity (23.47 at 6 ppm), low limit of detection (LOD) (237 ppb), optimal selectivity, and outstanding long-term stability. Furthermore, the enhancing mechanism of gas sensing performance was substantiated through density functional theory (DFT) calculation, while the practical application for the evaluation of spoiled cooked rice was conducted as well. This study demonstrates a reliable method for detecting a VOC biomarker in cooked rice, which can ensure food security and improve palatability of cooked rice.

Keywords: tungsten trioxide (WO_3); gas sensor; doping; geranyl acetone; room temperature; density functional theory (DFT)

1 Introduction

Geranyl acetone with *magnolia* and green odor [1] is an essential biomarker for fragrance and freshness of cooked rice, which greatly affects palatability and acceptability of consumers [2,3]. The extraction and analysis of volatile organic compounds (VOCs) in packaged cooked rice by the gas chromatographic technique demonstrated that the concentration of geranyl acetone (*X*) decreased with prolongation of storage time, which was mainly caused by the oxidation of compounds due to residual oxygen in the package [4]. However, even though geranyl acetone is a common biomarker of diverse cooked rice, fruits, and plant diseases [5,6], there were few research methods on gas sensing properties for monitoring it, and the demands for accurate evaluation and nondestructive testing of early cooked rice spoilage at ppb level are tough to approach as well [7].

A semiconductor metal oxide (SMOX) gas sensor with characteristics of low loss, non-toxicity, real-time detection, and ease of production can effectively detect VOCs with low concentrations under different circumstances [8–10]. Tungsten trioxide (WO_3) is a significant SMOX material with an appropriate bandgap, high oxygen vacancies (O_V), and excellent

* Corresponding author.
E-mail: zhangc@yzu.edu.cn

electron transfer properties displaying highly stable, classical transition feature, different crystalline nanostructure, and high sensitivity [11–14], which has been widely used for VOC detection (Table S1 in the Electronic Supplementary Material (ESM)). However, WO_3 gas sensors have been facing challenges in practical applications on account of poor selectivity and required high operating temperatures. Therefore, abundant researchers devoted to the manufacture of cryogenic sensors [15], and relevant research has been in-depth developed to modify physicochemical nature of pristine WO_3 for solving the existing bottleneck. Among noble-metal sensitization [16], morphological control [17], metallic impurity doping [18], heterostructure construction [12], and other referential methods, doping metallic impurities is deemed as a feasible means to enhance gas sensing features [19]. Specifically, doping with Fe^{3+} in SMOX can boost the optical band-gap width and conductivity, meanwhile modifying electronic structures and surface chemical states of materials [20], thereby strengthening VOC sensing applications of SMOX [21].

In this context, we reported the WO_3 nanoparticles doped with certain amounts of iron (Fe) ions (0%, 2%, 3%, 4%, and 5%) contributing to ultrasensitive sensing performance by combing the properties of low limit of detection (LOD) (237 ppb), excellent sensitivity (~23.47), fast response (~41 s), and favorable long-term stability for 6 ppm geranyl acetone at room temperature. The density functional theory (DFT) and valence band X-ray photoelectron spectroscopy (VB-XPS) analysis were carried out for elaborating on the sensing enhancement mechanism. In addition, the practicality was verified by studying early spoilage conditions of cooked rice by the as-prepared optimal sensors. The investigation and acquired findings put forward a novel candidate for monitoring characterized VOCs generated from cooked rice under different conditions, which probably ameliorates rice cooking methods, affects packaged cooked rice industry positively, and improves palatability for consumers.

2 Materials and methods

All the chemicals utilized in experiments pertained to the analytical grade and were directly utilized without any purification. Sodium tungstate dihydrate ($Na_2WO_4{\cdot}2H_2O$) (≥ 99.5%) and HNO_3 (65–68 wt%) were purchased from Sinopharm Chemical Reagent Co., Ltd. Anhydrous ferric chloride ($FeCl_3$) (≥ 98%) was obtained from Anhui Senrise Technology Co., Ltd. Anhydrous ethanol was acquired from Chinasun Specialty Products Co., Ltd.

2.1 Synthesis of Fe-doped WO_{3-x} nanoparticles

Pristine WO_3 and Fe-doped WO_{3-x} nanoparticles were obtained through a facile one-step solvothermal reaction (Fig. S1 in the ESM). In a concrete process, 2 mmol $Na_2WO_4{\cdot}2H_2O$ was dissolved and dispersed in a commixture of 20 mL deionized water and 30 mL HNO_3 (65 wt%) followed by stirring vigorously for 20 min. The final solution was moved into a Teflon-lined stainless autoclave (100 mL) and subsequently kept at 160 ℃ for 10 h. After cooling down to ambient temperature, the precipitates were washed with deionized water and absolute alcohol alternatively, and finally dried at 60 ℃ for 16 h. For improving crystallinity of WO_3, the obtained powders were calcined at 550 ℃ for 3 h at a ramp rate of 2 ℃·min^{-1}. As for Fe–WO_{3-x} samples, the preparation procedure is the same except that $FeCl_3$ of different amounts are added in the first step of the synthesis. The samples prepared by adding 0, 0.0054, 0.0081, 0.0108, and 0.0135 g of $FeCl_3$ were nominated as WO_3, 2% Fe–WO_{3-x}, 3% Fe–WO_{3-x}, 4% Fe–WO_{3-x}, and 5% Fe–WO_{3-x}, respectively, which are based on the molar ratios of Fe^{3+} to W^{6+}. All samples presented a flaxen color as abundant O_V.

2.2 Material characterization

Phase identification and crystal forms of the samples were gained by an X-ray diffractometer (D8 Advance, Bruker), and the micromorphology analysis was obtained by a field emission-scanning electron microscope (FE-SEM; S4800, Hitachi), a transmission electron microscope (TEM; G2 F30 S-TWIN, Tecnai), and an atomic force microscope (AFM; SPM-9700HT, Shimadzu). Ultraviolet–visible (UV–Vis) absorption spectra and bandgap were obtained via an ultraviolet–visible–near infrared (UV–Vis–NIR) spectrophotometer (Cary 5000, Varian). Chemical states of relevant elements and their distribution uniformity were observed via an X-ray photoelectron spectrometer (ESCALAB 250Xi, Thermo Scientific) and a high-angle annular dark-field scanning transmission electron microscope (HAADF-STEM) combined with an energy dispersive spectrometer, respectively. The X-ray photoelectron spectrometer

was calibrated with binding energy of the C 1s peak (284.8 eV). The surface O_V was confirmed through an electron paramagnetic resonance (EPR) spectrometer (A300-10/12, Bruker), while rotational and vibrational modes and photoluminescence (PL) spectroscopy were analyzed by Raman spectrometer (Renishaw inVia). Brunauer–Emmett–Teller (BET) surface area with N_2 adsorption/desorption isotherms and pore-size distribution was investigated via a specific surface and aperture analyzer (Autosorb IQ3, Quantachrome Instruments).

2. 3 Gas sensing setup and sensor characterization

All sensors were fabricated by mixing the powders with deionized water, and then ground to generate uniform pastes. The surfaces of the electrode were dip-coated by the homogenous pastes, and then dried at 130 ℃ for 24 h and further aged in a muffle furnace (KSL-1200X, HF-Kejing) at 200 ℃ for 72 h for thermal stabilization, avoiding the sensor signal drift. The experimental facilities employed in this investigation were the same as those reported in Refs. [22,23]. The real-time electrical resistance was presented via a gas tester (SD 101, Wuhan Huachuang Ruike Technology Co., Ltd.). The response of the gas sensor (S) utilized in this work is defined by Eq. (1):

$$S = R_a / R_g \tag{1}$$

where R_a and R_g represent the resistance of the gas sensor after exposure to pure air (79% N_2 + 21% O_2) and geranyl acetone, respectively. Additionally, the response/recovery time (τ_{res}/τ_{rec}) was obtained according to the duration reaching 90% of the resistance variation of the fabricated sensor during the adsorption and desorption of geranyl acetone molecules, respectively.

In the experiments, the flow rate of the vapor and the static and dynamic test conditions need to be accurately controlled, as the sensor response will be affected by the heat exchange process between itself and surrounding vapor [24]. More details for the gas sensing setup and practicability applications are provided in Section S2 in the ESM.

3 Results and discussion

3. 1 Characterization results

Crystal phase compositions and fineness of the as-synthesized materials were investigated via X-ray diffraction (XRD). As shown in Fig. 1(a), all diffraction peaks of the as-prepared samples were well indexed to the standard card of monoclinic phase WO_3 (space group: $P21/a$, JCPDS No. 05-0363), while the peaks of monoclinic WO_3 appear at 23.175°, 23.631°, 24.421°, 26.652°, 29.005°, 33.357°, 34.236°, and 42.010° corresponding to the (001), (020), (200), (120), (111), (021), (220), and (221) planes, respectively. Moreover, the d-spacing values and crystallite sizes (D) of the as-prepared samples can be obtained by Bragg equation [22] (Eq. (2)) and Scherrer equation [25] (Eq. (3)), respectively, as listed in Table 1, while the full width at half maximum (FWHM) and peak positions of the following XRD patterns were calculated by a multi-peak fitting using Gaussian algorithm.

$$2d_{hkl}\sin\theta = n\lambda \tag{2}$$

$$D = \frac{k\lambda}{\beta\cos\theta} \tag{3}$$

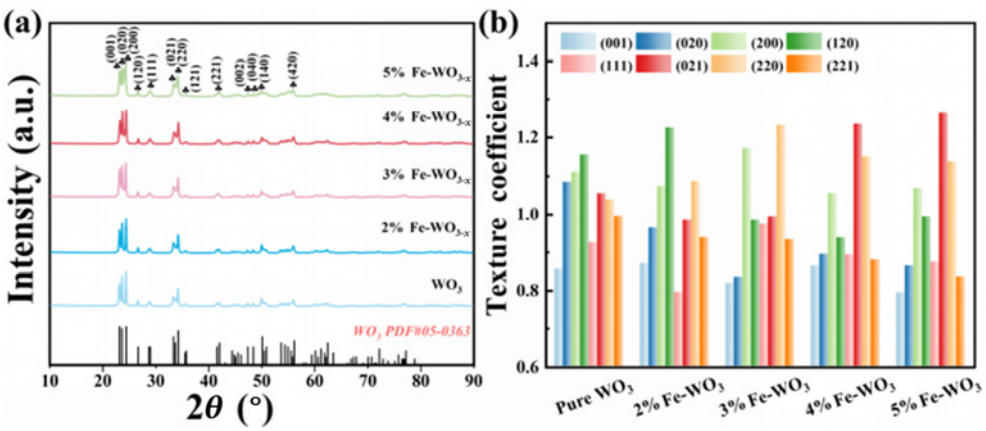

Fig. 1 (a) XRD patterns of WO_3, 2% Fe–WO_{3-x}, 3% Fe–WO_{3-x}, 4% Fe–WO_{3-x}, and 5% Fe–WO_{3-x}; (b) texture coefficient ($TC_{(hkl)}$) values of all samples.

Table 1 Structural parameters of as-prepared samples

Sample	Cell parameter (Å)			Cell volume (Å^3)	D (nm)
	a	b	c		
WO_3	7.287	7.517	3.836	210.122	23.90
2% Fe–WO_{3-x}	7.285	7.516	3.834	209.927	24.43
3% Fe–WO_{3-x}	7.283	7.514	3.831	209.649	19.45
4% Fe–WO_{3-x}	7.282	7.511	3.829	209.428	20.10
5% Fe–WO_{3-x}	7.280	7.509	3.826	209.150	24.39

where θ refers to the Bragg angle, β represents the FWHM (in rad), k (= 0.94) refers to the shape factor, and λ (= 0.15406 nm) refers to the wavelength of X-ray source. n represents the diffraction order (for the first order, n = 1), while d_{hkl} is the interplanar spacing (in Å). Specifically, no characteristic peaks arising from Fe metal are detected in Fe-doped WO_{3-x}, indicating that the Fe content of doping is too low, or Fe ions are embedded into the crystal lattice of WO_3. Then, the valence states of the embedded Fe ions were further verified. As the ionic radii of W^{6+}, Fe^{3+}, and Fe^{2+} are 0.0600, 0.0550, and 0.0630 nm, respectively [26,27], the replacement of W^{6+} ions in WO_3 with larger metal ions will contribute to the enlargement of a crystal cell [28]. As the synthesized Fe-doped WO_{3-x} belongs to the monoclinic crystal system, the lattice constants (a, b, and c) can be obtained by Eq. (4), as listed in Table 1.

$$\frac{1}{d_{hkl}^2} = \frac{\dfrac{h^2}{a^2}+\dfrac{k^2}{b^2}+\dfrac{l^2\sin^2\gamma}{c^2}-\dfrac{2hk\cos\gamma}{ab}}{1-\cos^2\gamma} = \frac{h^2}{a^2\sin^2\gamma}+\frac{k^2}{b^2\sin^2\gamma}+\frac{l^2}{c^2}-\frac{2hk\cos\gamma}{ab\sin^2\gamma}\gamma \quad (4)$$

where h, k, and l refer to the crystal face index, and γ is an angle in the lattice constant. Notably, the lattice parameters and cell volumes of the samples reduced gradually with the rising concentration of the Fe dopant, illustrating that Fe^{3+} was successfully doped into the lattice of WO_3.

Furthermore, the $TC_{(hkl)}$ parameters are obtained by Eq. (5) for further explanation [29,30]:

$$TC_{(hkl)} = \frac{I_{(hkl)}/I_{0(hkl)}}{\dfrac{1}{N}\sum I_{(hkl)}/I_{0(hkl)}} \quad (5)$$

where $I_{(hkl)}$ and $I_{0(hkl)}$ refer to the relative and standard peak intensities in XRD patterns, respectively, and N refers to the reflection number. The calculated TC values and their corresponding variations are shown in Table S2 in the ESM and Fig. 1(b), respectively. Different amounts of doping may cause re-orientation effect, manifesting that the (200), (111), and (220) planes got preferential growth, as shown in Fig. 1(b). The TC values of the (200), (111), and (220) planes reached the maximum values of 1.1708, 0.9733, and 1.2318 in 3% Fe–WO_{3-x}, respectively, while the increasing amounts of Fe doping caused a transformation in the preferred orientation to the (021) plane in the 5% Fe–WO_{3-x} sample. In detail, the surface energy sequence of monoclinic WO_3 is (020) < (200) < (220). Consequently, taking advantage of changing Fe doping contents makes specific exposed facets possess higher surface energy, enhancing physical–chemical activity of sensing materials [31].

Morphologies and microstructures of WO_3 and Fe-doped WO_{3-x} were inspected via FE-SEM and high-resolution TEM (HRTEM), respectively. As shown in Fig. 2(a) and Fig. S3 in the ESM, all samples own the nanoparticle-like morphology, while the lengths of the nanoparticles are around 50–150 nm. The average particle size of 3% Fe–WO_{3-x} is around 110 nm, as shown in Fig. S4 in the ESM, and all Fe-doped WO_{3-x} nanoparticle-liked samples distinctly displayed flat and smooth features with wrinkling. AFM images with a non-contact mode are taken in Fig. S5 in the ESM. As the thicknesses of WO_3 and 3% Fe–WO_{3-x} are both ~25 nm, the doping of Fe^{3+} represents no apparent impact on the microstructure of different samples. From the HRTEM results (Figs. 2(b)–2(e)), nanoparticle-like 3% Fe–WO_{3-x} was displayed, and the HRTEM images along with a homologous selected area electron diffraction (SAED) pattern, which is shown in Fig. 2(f), were obtained from a random optional field. The diffraction ring of the SAED pattern does not exist, which indicated the single crystal property of Fe-doped WO_{3-x} nanoparticles [32]. In addition, the contrast of Fe vs. W cations can be seen in intensity profiles (Fig. S6 in the ESM) obtained from the marked area "1" of 3% Fe–WO_{3-x}, which indicated good doping of the Fe ions [33]. Energy dispersive spectroscopy (EDS) elemental mappings (Figs. 2(g)–2(i)) demonstrate the presence of W, O, and fewer Fe, which were homogeneously distributed among the nanoparticles.

Raman spectra were depicted for acquiring molecular structures and compositions of all samples. Two Raman peaks centered at 680 and 803 cm^{-1} were attributed to the O–W–O modes, while the peak around

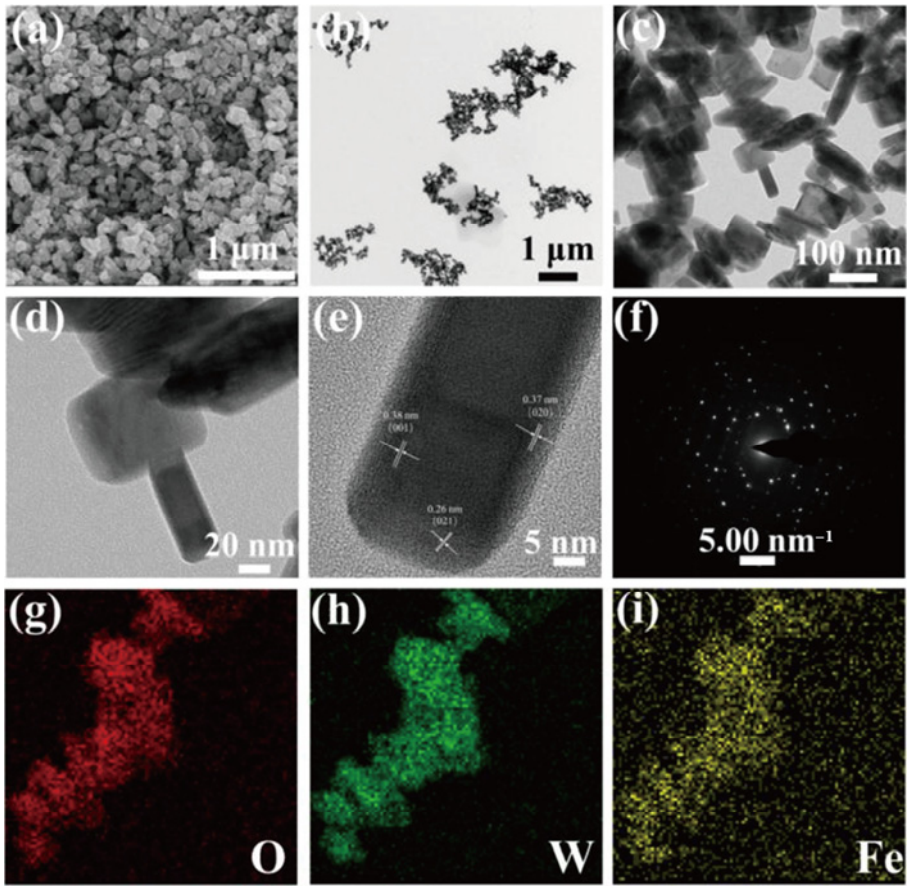

Fig. 2 (a, b) FE-SEM images of 3% Fe–WO_{3-x}; (c, d) HRTEM images of 3% Fe–WO_{3-x}; (e) lattice distances of various crystal planes of 3% Fe–WO_{3-x}; (f) SAED pattern of 3% Fe–WO_{3-x}; (g–i) STEM–EDS mappings of O, W, and Fe of 3% Fe–WO_{3-x}.

267 cm^{-1} may assign to bending vibration of δ(O–W–O), which is shown in Fig. 3(a) [34]. As a result, the crystal structures of the samples may comprise a network within homocentric WO_6 octahedron elements, which constitute O–W–O microcrystalline clusters that are interconnected by W–O–W, with the terminal W=O bonds at the surface of the clusters [35]. As evident in Fig. 3(b), adsorption–desorption isotherms of 3% Fe–WO_{3-x} are attributed to type-IV isotherms according to International Union of Pure and Applied Chemistry (IUPAC) classification, and the specific surface area of 3% Fe–WO_{3-x} is up to 25.729 $m^2 \cdot g^{-1}$, contributing to providing rich oxygen adsorption sites and further facilitating carrier transportation. Pore-size distribution curves (Fig. 3(c)) demonstrate that 3% Fe–WO_{3-x} was assigned to mesoporous materials with an average pore diameter of 3.139 nm. Furthermore, other BET test results of the as-synthesized samples are listed in Table S3 in the ESM.

Optical bandgaps of all samples were analyzed by the UV–Vis testing. Specifically, the light absorption edge wavelengths of five samples are in the range of approximately 502.87–514.23 nm, as shown in the inset of Fig. 3(d). The E_g values are calculated by Kubelka–Munk equation (Eq. (6)) [36] and demonstrated in Fig. 3(d). 3% Fe–WO_{3-x} owns the narrowest bandgap of 2.42 eV, which will accelerate the electron transition speed, thereby enhancing the sensing performance.

$$\alpha hv = A(hv - E_g)^{m/2} \tag{6}$$

where A is an integer, and the value of m for WO_3 is 1 due to its direct optical transition type. The elemental composition was evaluated via XPS. All the Fe–WO_{3-x} samples contained the corresponding elements including Fe, W, and O (Fig. 4(a)). The chemical states of the Fe ions in the 3% Fe–WO_{3-x} nanoparticles are explored in Fig. 4(b). The characteristic peaks at 724.38 and 710.22 eV indexed well to Fe $2p_{1/2}$ and Fe $2p_{3/2}$, respectively, while satellite peaks at ca. 732.46 and 718.40 eV were corresponding to the Fe^{3+} species [37]. Furthermore, the O 1s peaks (Fig .4(c)) can generally be divided into three kinds of oxygen species for both

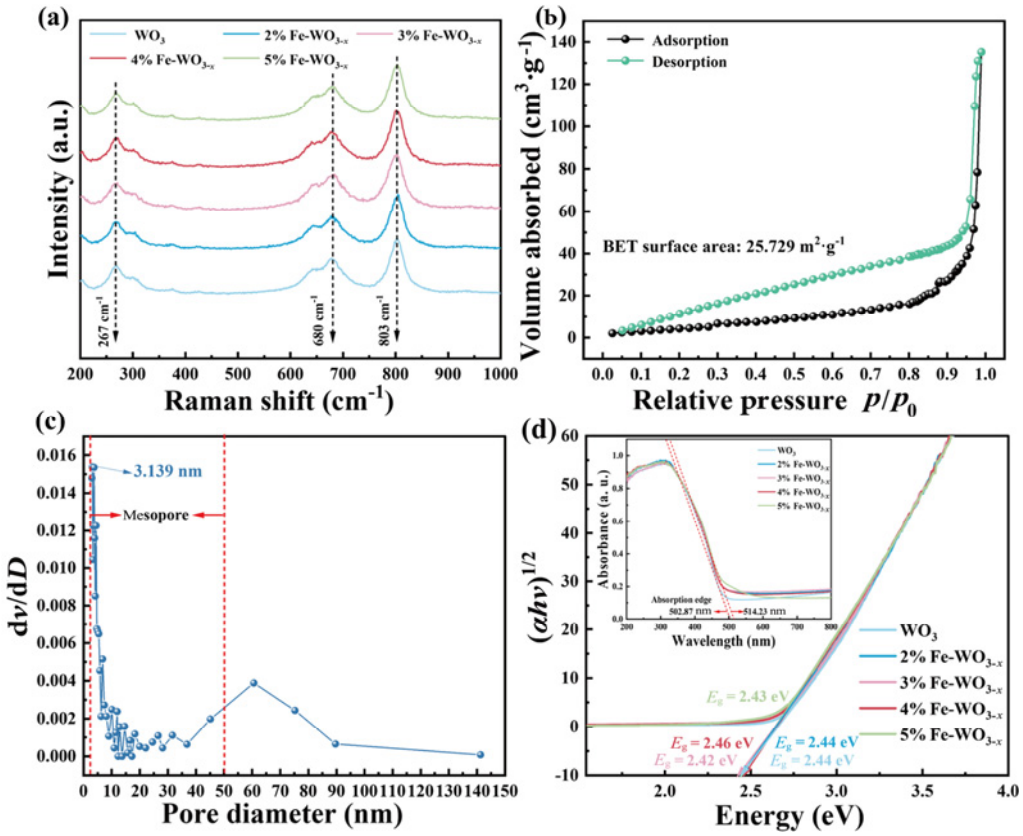

Fig. 3 (a) Raman spectra of all samples; (b) N_2 adsorption–desorption isotherms of 3% Fe–WO_{3-x} where p is the true pressure of the gas, and p_0 is the saturated vapor pressure of the gas at the measured temperature; (c) pore-size distribution of 3% Fe–WO_{3-x}; (d) calculated band-gap energies (E_g) of all samples (the inset is the UV–Vis diffuse absorbance spectra of all samples).

pure WO_3 and 3% Fe–WO_{3-x}, which are the lattice oxygen (O_L), O_V, and chemisorbed oxygen (O_C). In detail, O_L, O_V, and O_C of WO_3 and 3% Fe–WO_{3-x} are 530.28, 530.78, and 531.86 eV and 529.96, 530.39, and 531.44 eV, respectively. The proportions of O_V and O_C in 3% Fe–WO_{3-x} were higher than those of pristine WO_3, which enhanced the gas sensing performance for that O_V motivated numerous active gas adsorption sites and accelerated the reaction between the target VOC molecule and the surface of the sensing materials, while O_C primarily participated in the surface redox reaction of the VOC molecules onto the SMOX materials [38]. As shown in Fig. 4(d), W 4f can be divided into two specific peaks located at 37.75 and 35.60 eV assigned to W $4f_{5/2}$ and W $4f_{7/2}$, respectively. As for 3% Fe–WO_{3-x}, the declined binding energy of W 4f (37.46 and 35.30 eV for W $4f_{5/2}$ and W $4f_{7/2}$, respectively) revealed that the incorporation of the Fe^{3+} ions in the crystalline structure of the samples replaced W^{6+} ions, in line with the XRD results [39]. These results indicated that the Fe ions consist in the WO_3 nanoparticles via a fast and facile method, and Fe-doped WO_{3-x} may enhance the gas sensing performance under real testing conditions.

As illustrated in Fig. 4(e), the PL spectra indicated that the addition of the Fe contents increased the concentration of O_V. Furthermore, EPR signals of five samples display one peak consistent with a g factor (the g value represents the factor of a free radical or unpaired electron in the EPR spectrum) of 2.003, as shown in Fig. 4(f). The results further demonstrate that there existing larger number of O_V in 3% Fe–WO_{3-x} samples, which is believed that the enhancement of the signal was derived from the production of W^{5+} [40]. Specifically, O_V can localize electrons, which will transfer to W^{6+}, leading to the generation of W^{5+} [41].

3. 2 Gas sensing performance

The sensing performance of pristine WO_3 and Fe–WO_{3-x} nanoparticles was investigated under room-temperature conditions (25±2 ℃). First of all, the 3% Fe–WO_{3-x} gas sensor was tested by exposing them to 8 ppm geranyl acetone at different working temperatures. The response declined as the working

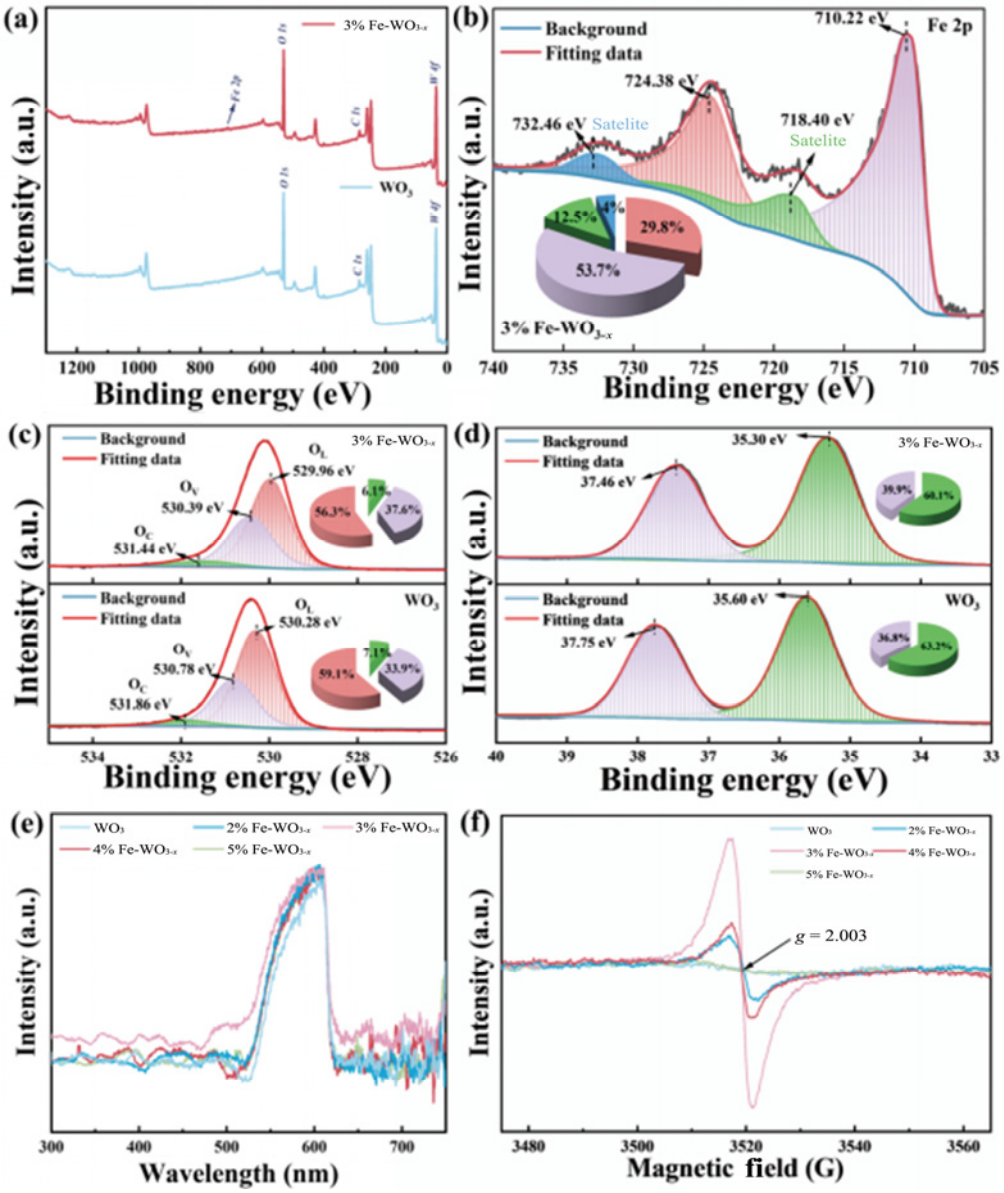

Fig. 4 Element chemical states of pristine WO_3 and 3% Fe–WO_{3-x} composite determined by XPS: (a) survey spectra; (b) Fe 2p spectra; (c) O 1s spectra; (d) W 4f spectra. (e) PL spectra and (f) EPR measurement at room temperature of all samples.

temperature increased between room temperature and 100 ℃ (Fig. S7 in the ESM), suggesting that room temperature is the optimal selection for gas sensing. Figures 5(a) and 5(b) and Fig. S8 in the ESM depict the transient gas sensing characteristic of the as-fabricated gas sensors at diverse concentrations of geranyl acetone ranging from 2 to 10 ppm. Above all, the transient response–recovery behavior reveals reversible and relatively stable sensing properties of Fe-doped WO_{3-x} onto geranyl acetone, and the 3% Fe–WO_{3-x} sensor owns the greatest response values (2.42, 10.65, 23.47, 41.32, and 82.7 at 2, 4, 6, 8, and 10 ppm geranyl acetone, respectively) compared with those of other gas sensors made in the same batch. Furthermore, the response values of all gas sensors came up equably when X is increased, which are listed in Table S7 in the ESM. The relationship of 3% Fe–WO_{3-x} gas sensor response values (Y) vs. X (Fig. 5(c)) abides by a stepwise distribution, and it can be fitted by the typical parabola relation:

$$Y = AX^2 + BX + C \quad (7)$$

where A represents the quadratic term coefficient, B represents the first-order coefficient, and C represents a constant term. On the fundament of the parabola law, A, B, and C are 1.281, −5.975, and 12.088, respectively. For evaluating the reproducibility of the gas sensors,

Fig. 5(d) illustrates 5 cycles of the 3% Fe–WO_{3-x} gas sensor towards 6 ppm geranyl acetone, while the response values maintained around 24.5, and the corresponding standard deviation is 0.54. As shown in Figs. 5(e) and 5(f), the transient response curves of 3% Fe–WO_{3-x} and pure WO_3 exhibit τ_{res}/τ_{rec} of 41 s/480 s and 56 s/383 s, respectively. The long-term stability was tested by inletting 6 ppm geranyl acetone to 2% Fe–WO_{3-x} and 3% Fe–WO_{3-x} sensors for one month. As shown in Fig. 5(g), the error bar with a fill area of response stable characteristic illustrated that there was almost no variation in the response value within one month. Furthermore, the cross selectivity has always been vulnerability that is difficult to overcome due to the inherent sensing principle of the SMOX gas sensors. Thus, we explored the selectivity by calculating the selectivity coefficient (K), as shown in Fig. 5(h), and the gas concentration was kept at 10 ppm, while the equation is shown by Eq. (8) [42]:

$$K = \frac{S_{\text{target gas}}}{S_{\text{interference gas}}} \tag{8}$$

where $S_{\text{target gas}}$ and $S_{\text{interference gas}}$ are the response of the target gas and the interference gas, respectively.

For the WO_3 gas sensor, K was calculated to be 2.80, 3.59, 3.97, 5.01, 5.48, 5.75, and 6.76 for nonanal, 1-octen-3-ol, 2-pentylfuran, ethanol, hexanal, linalool, and pyridine, respectively, while the corresponding

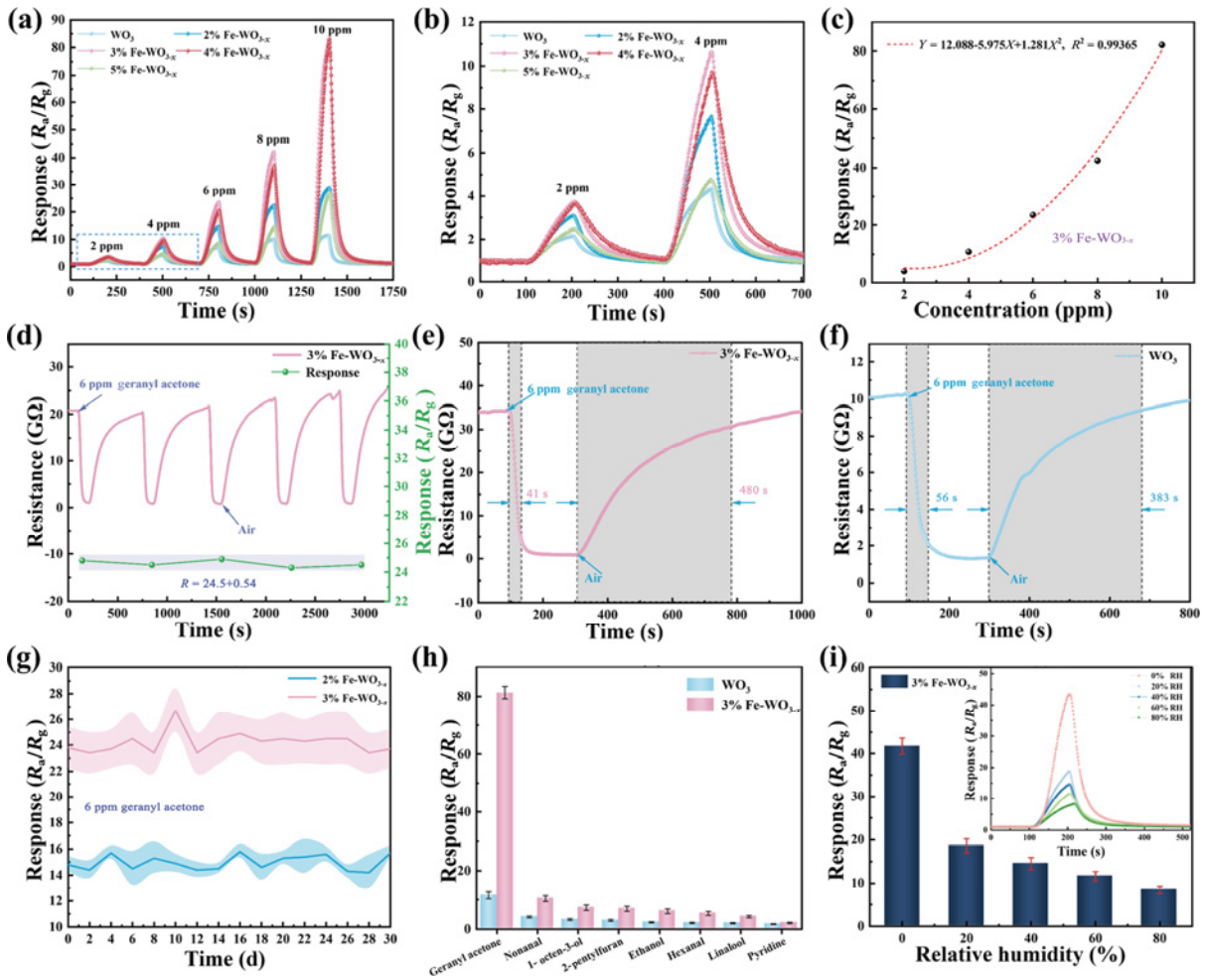

Fig. 5 (a) Dynamic response/recovery curves of five samples to 2–10 ppm geranyl acetone at room temperature; (b) dynamic response/recovery curves of five samples to 2–4 ppm geranyl acetone at room temperature; (c) relationship of Y vs. X where R^2 is the coefficient of determination to evaluate the goodness of fit of the regression model coefficients; (d) response to 6 ppm geranyl acetone of 3% Fe–WO_{3-x} in 5 cycles; (e) τ_{res}/τ_{rec} of 3% Fe–WO_{3-x} to 6 ppm geranyl acetone at room temperature; (f) τ_{res}/τ_{rec} of WO_3 to 6 ppm geranyl acetone at room temperature; (g) error bars with fill area of response stable characteristic of 2% Fe–WO_{3-x} and 3% Fe–WO_{3-x} sensor to 6 ppm geranyl acetone in one month; (h) selectivity to 10 ppm geranyl acetone and various gases of WO_3 and 3% Fe–WO_{3-x} at room temperature (error bar (o) = 3); (i) variation of response values and baseline resistance vs. relative humidity (RH) of 3% Fe–WO_{3-x} (error bar (o) = 3) (the inset is corresponding response/recovery curves 3% Fe–WO_{3-x} to 8 ppm geranyl acetone under different RHs).

results are 7.82, 11.14, 11.78, 13.33, 15.34, 19.36, and 38.71, respectively, for the 3% Fe–WO_{3-x} gas sensor. The data acquired from the 3% Fe–WO_{3-x} gas sensor processed outstanding selectivity towards 10 ppm geranyl acetone at room temperature.

In a real test environment, RH can vary from 5% to 95% with accuracy of ±2.5% [43], and thus the response values of the 3% Fe–WO_{3-x} gas sensor under different RHs are shown in Fig. 5(i). When RH increased from 20% to 80%, the sensitivity decreased due to adsorbed water molecules, restricting the efficient adsorption of oxygen and geranyl acetone molecules. Above all, the reduced adsorbed geranyl acetone molecules bring about a declining response in higher humidity.

In detection circumstances of real cooked rice flavor, X is as low as ppm or ppb level, and thus LOD of the as-prepared gas sensor should be probed [22]. The details about the LOD calculation are given in Section S3 in the ESM. Thus, LODs of WO_3 and 3% Fe–WO_{3-x} were 431 and 237 ppb respectively, which revealed the excellent practical application of the room-temperature geranyl acetone sensor.

3. 3 Gas sensing mechanism

An intuitive scheme for sensing enhancement mechanism of the WO_3 sensor for geranyl acetone vapor is provided in Fig. 6(a). Once sensors expose themselves to high-purity air, some oxygen molecules will be absorbed by the sensing materials chemically, while the electrons located at the conduction band (CB) were retrieved to form O_2^- at room temperature (Reactions (9) and (10), respectively). Therefore, the electron depletion layer becomes thinner, and the bending of the energy band can be illustrated by the rising of the sensing material resistance. After injecting the target VOC (geranyl acetone) into a gas chamber, the geranyl acetone molecule combined with oxygen species to generate the electrons, which will return to CB (Reaction (11)), narrowing the electron depletion layer and further increasing the conductivity of the materials [44,45]. Therefore, the variation of the gas sensor resistance proved that the as-fabricated gas sensors are appropriate for detecting low concentrations of geranyl acetone.

$$O_2(\text{gas}) \leftrightarrow O_2(\text{ads}) \quad (9)$$

$$O_2(\text{ads})+e^- \leftrightarrow O_2^-(\text{ads}) \ (\text{temperature} < 150\ ℃) \quad (10)$$

$$C_{13}H_{22}O(\text{gas})+18O_2^- \rightarrow 13CO_2(\text{gas})+11H_2O+18e^- \quad (11)$$

As Fe^{3+} replaces W^{6+}, some O_V are induced accompanied by the Fe doping based on the defect model using Kröger–Vink reaction (Reaction (12)). Specifically, O_V are ulteriorly ionized into second-order-ionized O_V ($V_{Ö}$), and adsorbed oxygen will capture more free electrons by intensifying the surface redox reaction of VOC molecules onto the sensing materials and further improving the gas sensor performance (Reaction (13)) [46].

$$WO_3 \rightarrow W_{Fe}+O_O \quad (12)$$

$$O_O \rightarrow V_{Ö}+1/2O_2+2e^- \quad (13)$$

where O_O is the specific concentration of the oxygen vacancy which is induced by Fe-doping. To further explore the enhanced sensing mechanism, the CB potential of the samples (E_{CB}) is calculated below, and the VB potential can be obtained via the VB-XPS technique ($E_{VB,XPS}$, Figs. 6(b)–6(d)). Therefore, $E_{VB,XPS}$ of WO_3 and 3% Fe–WO_{3-x} are 2.22 and 1.84 eV, respectively.

$$E_{VB,NHE} = \varphi + E_{VB,XPS} - 4.44 \quad (14)$$

where φ (= 4.52 eV) represents the work function of the XPS tester. Therefore, the VB potential obtained by the normal hydrogen electrode ($E_{VB,NHE}$) of WO_3 and 3% Fe–WO_{3-x} are calculated to be 2.30 and 1.92 eV, respectively (Eq. (14)). Furthermore, the relationship between the work function in Φ and ΔV is shown in Eq. (15) [47]:

$$\Delta V = \Phi - \varphi \quad (15)$$

where ΔV refers to the distance between adjacent IPs (Figs. 6(c) and 6(d)). Thus, Φ of WO_3 and 3% Fe–WO_{3-x} are 5.82 and 6.60 eV, respectively, and then the band structures can be obtained (Fig. 6(e)). Combined with all characterization assays and gas sensitivity tests, by adjusting the Fe doping content during the preparation of WO_3, O_V is regulated, and the band structure of metal oxide materials is changed. Comparing 3% Fe–WO_{3-x} with WO_3, as the concentration of O_V increases, the resulting free electrons will generate a new donor energy level in the forbidden band. Then hybridization occurs when the new donor level is in contact with VB, and the top of VB expands and shifts upward, thereby narrowing the bandgap [48].

Furthermore, the increase of the solvothermal temperature magnifies the Fermi level by 0.78 eV, indicating the improvement of charge carrier compensation from the establishment of the nanosheet

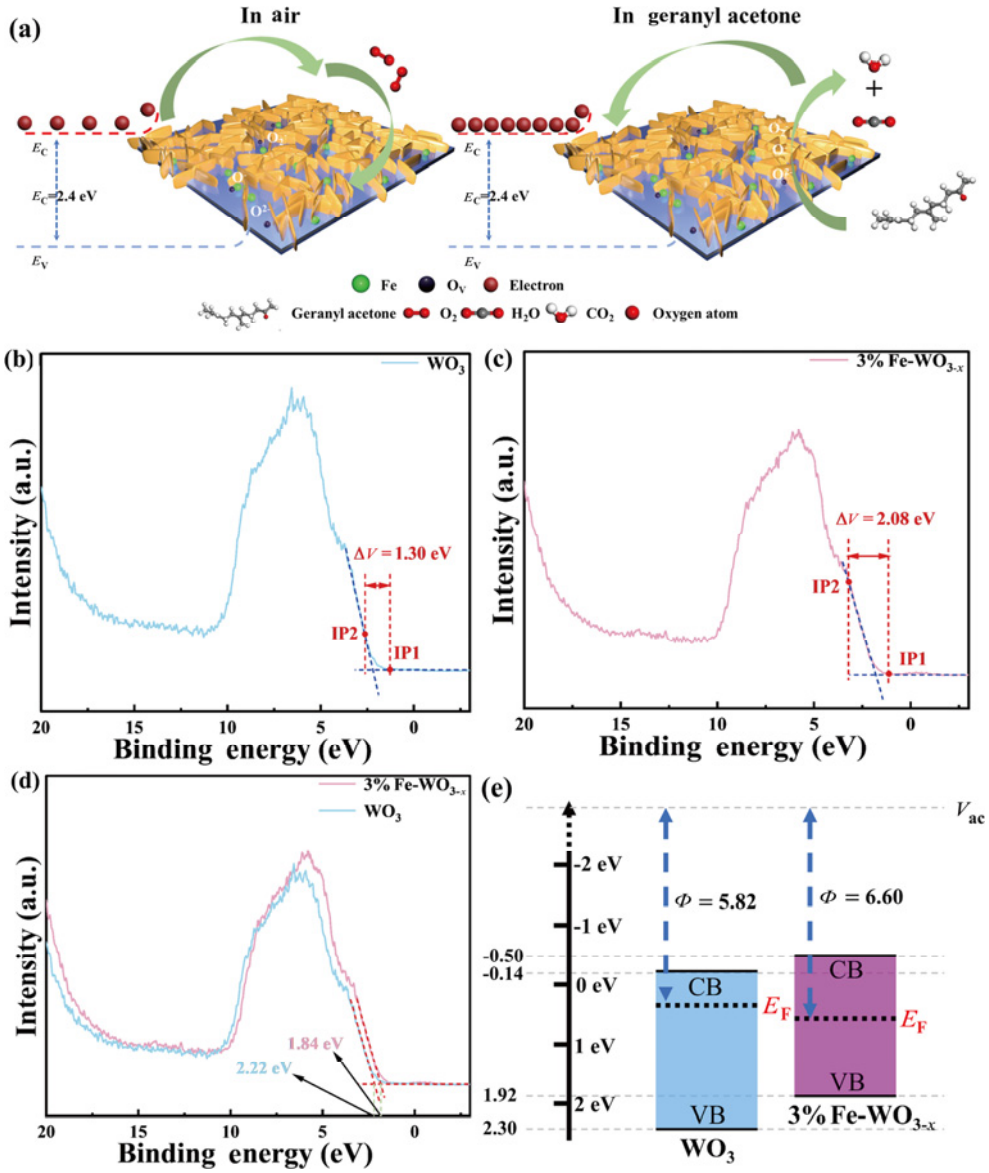

Fig. 6 (a) Schematic illustration of gas sensing mechanism for Fe-doped WO_{3-x}; work functions of (b) WO_3 and (c) 3% Fe–WO_{3-x}; (d) VB-XPS spectra of WO_3 and 3% Fe–WO_{3-x}; (e) band structures of WO_3 and 3% Fe–WO_{3-x}. Note: E_C and E_V are the energy of CB and VB, respectively, IP is the abbreviation of inflection point, ΔV is the contact potential difference, V_{ac} is the vacuum level which is defined as the energy level at which electrons are not attracted to nucleus and become free electrons, E_F is the energy of Fermi level, and Φ is the actual VOC detection.

heterojunction, which results in better geranyl acetone sensing performance.

To further explore the gas sensing mechanism for geranyl acetone to WO_3 and Fe–WO_{3-x}, the adsorption reaction between the geranyl acetone molecules and the surface of the as-prepared materials was simulated through Cambridge Sequential Total Energy Package (CASTEP) modules, and other setting details of the DFT calculation are given in Section S4 in the ESM. After surface cleaving of optimal WO_3 and Fe–WO_{3-x} crystals, the adsorption energy of the geranyl acetone molecules on WO_3 (011) and Fe–WO_{3-x} (011) (E_{ads}) can be calculated by Eq. (16):

$$E_{ads} = E_{total} - (E_{(011)} + E_{geranyl\ acetone}) \quad (16)$$

where E_{total} refers to the total energy of the geranyl acetone molecules absorbed on the certain crystal facet of the WO_3 and Fe–WO_{3-x} surface systems, $E_{(011)}$ is the energy towards (011) WO_3 and Fe–WO_{3-x} surface, and $E_{geranyl\ acetone}$ refers to the energy of the isolated geranyl acetone molecules.

As evident in Figs. 7(a) and 7(b), the calculated E_g

values of WO_3 and Fe–WO_{3-x} are 1.52 and 1.15 eV, respectively, indicating the formation of a narrower bandgap after the Fe doping, resulting from that the relatively bigger change of the bandgap was displayed for the higher doping contents setting in simulation. Figures 8(c) and 8(d) are the optimized primitive crystal structures of WO_3 and Fe–WO_{3-x}, respectively. Furthermore, the density of states (DOSs) of WO_3 and Fe–WO_{3-x} are depicted in Figs. 7(c) and 7(d), respectively, which indicate that the VB maximums (VBMs) of WO_3 and Fe–WO_{3-x} are primarily comprised of the O 2p orbital, and the CB minimums (CBM) of WO_3 and Fe–WO_{3-x} are the constitutions of hybrid orbitals within W 5d and O 2p and W 5d, O 2p, and Fe 3d, respectively. The DOS results demonstrate that the electrons may originate from the O 2p orbitals of WO_3 and Fe–WO_{3-x}, and then can be further excited about the hybrid orbitals of W 5d, O 2p, and Fe 3d [49].

To obtain the adsorption energy, the geometry structures for geranyl acetone adsorption systems of

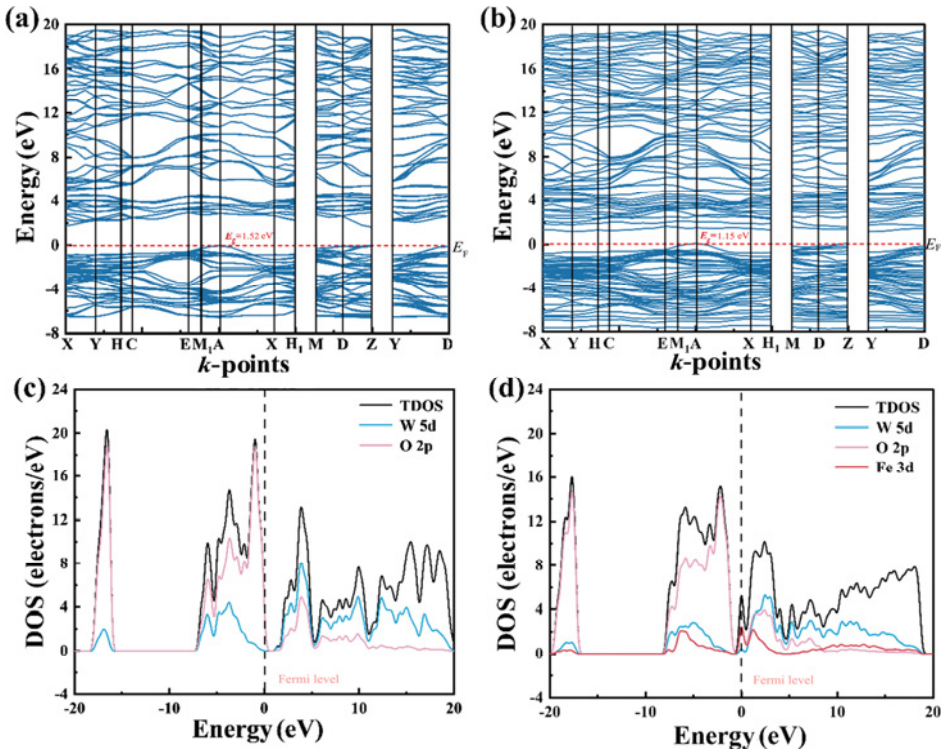

Fig. 7 Band structures of (a) WO_3 and (b) Fe–WO_{3-x} in monoclinic (MCL) lattice; DOSs of (c) WO_3 and (d) Fe-doped WO_{3-x} where TDOS is the abbreviation of total density of states.

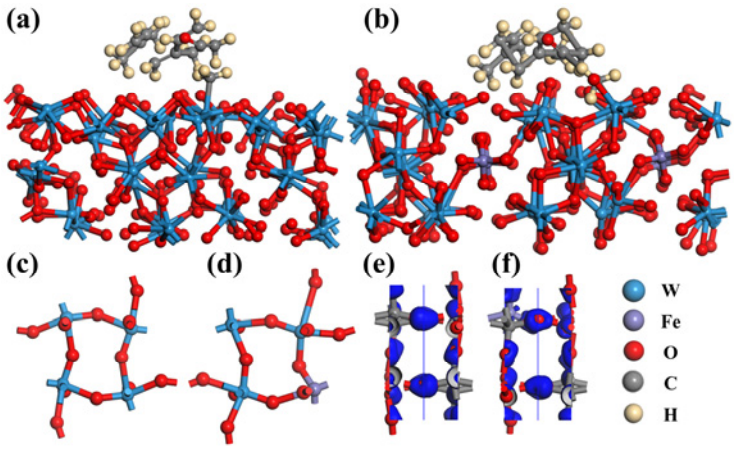

Fig. 8 Geometry structures for geranyl acetone adsorption systems of (a) WO_3 and (b) Fe-doped WO_{3-x}; geometry structures for (c) WO_3 and (d) Fe-doped WO_{3-x}; schematic diagrams of differential charge densities in geranyl acetone adsorption processes of (e) WO_3 and (f) Fe-doped WO_{3-x}.

WO_3 and Fe–WO_{3-x} are built in Figs. 8(a) and 8(b), respectively. The distances between geranyl acetone and WO_3 and Fe–WO_{3-x} matrices are 2.572 and 2.736 Å, respectively, while the corresponding adsorption energy is −0.95 and −1.23 eV, respectively, and the specific parameters of the two adsorption systems are listed in Table S10 in the ESM. The adsorption energy indicates the strongest binding of the geranyl acetone molecule to the Fe–WO_{3-x} surface, while the stronger adsorption energy reveals longer recovery time in the sensing test [50]. The same mode was applied to calculate the differential charge densities (Figs. 8(e) and 8(f)), indicating that the neighboring Fe site acts as an electron donor, promoting the electron transfer from WO_3 to the adsorbed geranyl acetone at the W site.

3. 4 Practicability application

The practicability application potential for the gas sensors prepared in this work was assessed under different storage conditions. During the storage process, the amount of released geranyl acetone molecules will decrease as cooked rice is prone to undergoing redox reaction and deterioration [4]. Herein, we combined the optimized 3% Fe–WO_{3-x} gas sensor with homemade gas sensing equipment to detect VOCs released from cooked rice, and the correlation diagrams are shown in Figs. S10 and S11 in the ESM. The response/recovery curves of the 3% Fe–WO_{3-x} gas sensor towards cooked rice under storage conditions at different duration (0, 6, 12, 18, and 24 h) are depicted in Figs. 9(a)–9(e). The response value decreased from 7.76 to 1.78 with longer storage time (Fig. 9(f)). For evaluating the freshness in different periods of cooked rice storage, according to the correlation between the concentration of the target gas and the response value of the 3% Fe–WO_{3-x} gas sensor, X volatilized from freshly cooked rice is about 3.75 ppm, of which with the prolonging of storage time, the VOC concentration will decline to the ppb level [51], which indicates that remaining cooked rice is highly spoiled after 24 h storage. Furthermore, the chemical reactions in cooked rice will decelerate under lower storage temperatures, resulting in few volatile oxidative products generated in cooked rice [2]. Therefore, the condition of the cooked rice storage at a low temperature was carried out (Fig. 9(f)). Cooked rice was stored at room temperature (25±2 ℃) and at a low temperature (−5±2 ℃) for 18 h, which demonstrated that the response value of the sensor corresponds to

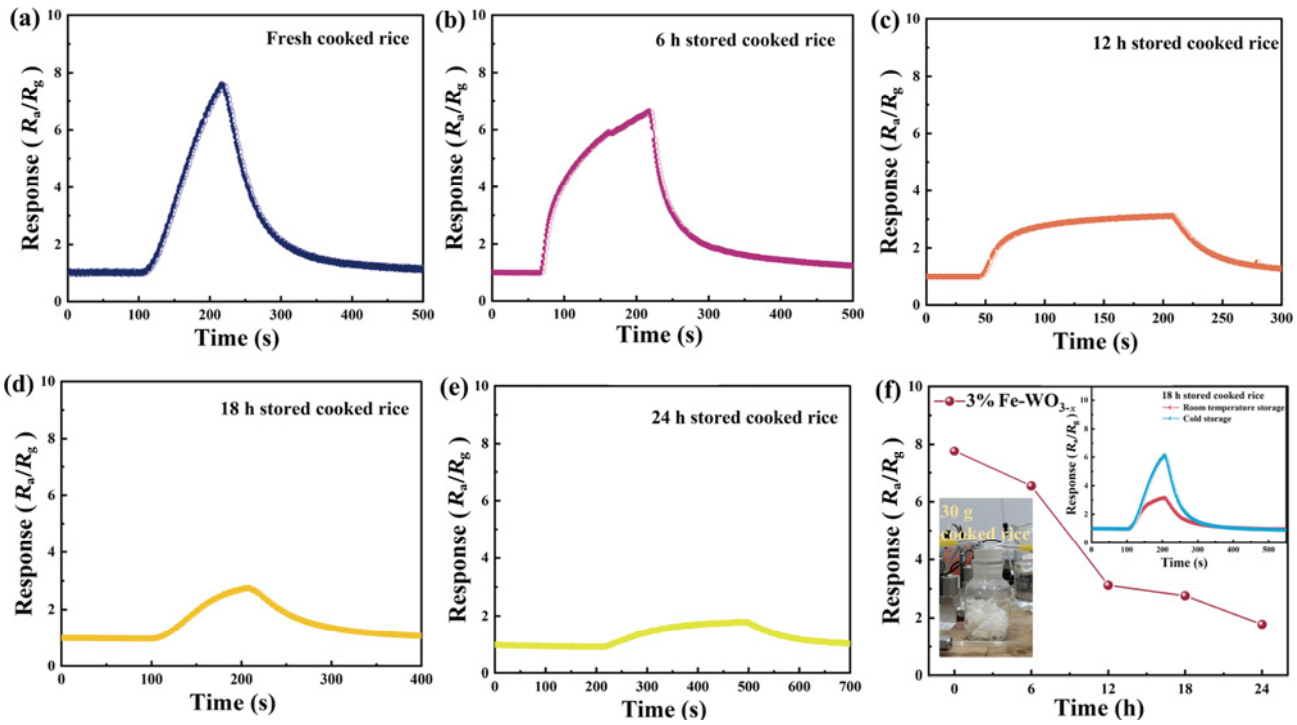

Fig. 9 (a–e) Response curves of 3% Fe–WO_{3-x} gas sensor towards released gases from 30 g cooked rice during different stages (0, 6, 12, 18, and 24 h); (f) response values of 3% Fe–WO_{3-x} gas sensor towards released gases from 30 g cooked rice during different stages (0, 6, 12, 18, and 24 h) (the inset in the top right corner is response curves of 3% Fe–WO_{3-x} gas sensors towards released gases from 30 g cooked rice during 18 h storage condition at room temperature and a low temperature).

3.13 and 6.10, respectively, indicating that cooked rice at a low temperature possessed a higher degree of freshness. Therefore, the 3% Fe–WO_{3-x} gas sensor possessed the promising potential for the detection of geranyl acetone and the quality inspection of cooked rice.

4 Conclusions

In conclusion, a novel and reliable geranyl acetone sensor based on WO_3 was created by a facile and economical solvothermal method. Fe ions were doped with WO_3 nanoparticles for high-performance geranyl acetone detection, and the response value is 7 times that for the WO_3 nanoparticles without Fe modification. The composite sensors presented outstanding response (2.42–82.7) toward 2–10 ppm geranyl acetone with low LOD (237 ppb), short τ_{res}/τ_{rec} (41 s/480 s) at room temperature, excellent selectivity, outstanding reproducibility, and long-term stability within 30 d. Strengthened sensing properties primarily contributed to the reduction in D, generous oxygen defects, advanced specific surface area, and promoted charge separation capacity of the fine-controlled Fe-doped WO_{3-x}. Additionally, the as-fabricated sensors were employed for geranyl acetone detection in cooked rice to verify the practicability application prospect in food spoilage monitoring. The multiple integrations of Fe-doped WO_{3-x} composites with other materials on the platform will be dealing with identifying multiple characterizing VOCs released from diverse food. Above all, the as-prepared gas sensor could be applied for rapid, precise, and reliable monitoring of geranyl acetone, which can facilitate the taste quality of cooked rice and is expected to be extended to cooked rice and other food detection for quality inspection.

Acknowledgements

This work was supported by the Outstanding Youth Foundation of Jiangsu Province of China (No. BK20211548), the National Natural Science Foundation of China (No. 51872254), and the Yangzhou City–Yangzhou University Cooperation Foundation (No. YZ2021153).

Declaration of competing interest

The authors have no competing interests to declare that are relevant to the content of this article.

Electronic Supplementary Material

Supplementary material is available in the online version of this article at https://doi.org/10.26599/JAC.2023.9220771.

References

[1] Yang DS, Shewfelt RL, Lee KS, *et al*. Comparison of odor-active compounds from six distinctly different rice flavor types. *J Agric Food Chem* 2008, **56**: 2780–2787.
[2] Li XJ, Han X, Gao GB, *et al*. Rice freshness determination during paddy storage based on solvent retention capacity. *Cereal Chem* 2022, **99**: 593–602.
[3] Bonikowski R, Świtakowska P, Kula J. Synthesis, odour evaluation and antimicrobial activity of some geranyl acetone and nerolidol analogues. *Flavour Frag J* 2015, **30**: 238–244.
[4] Tananuwong K, Lertsiri S. Changes in volatile aroma compounds of organic fragrant rice during storage under different conditions. *J Sci Food Agr* 2010, **90**: 1590–1596.
[5] Robinson MT, Tung J, Gharahcheshmeh MH, *et al*. Humidity-initiated gas sensors for volatile organic compounds sensing. *Adv Funct Mater* 2021, **31**: 2101310.
[6] Chen JN, Han HT, Liu CJ, *et al*. Characterization of aroma-active compounds in Dongli by quantitative descriptive analysis, gas chromatography–triple quadrupole tandem mass spectrometry, and gas chromatography–olfactometry. *J Food Sci Tech* 2022, **59**: 4108–4121.
[7] Zheng ZC, Zhang C, Liu KW, *et al*. Volatile organic compounds, evaluation methods and processing properties for cooked rice flavor. *Rice* 2022, **15**: 53.
[8] Zhang C, Huan YC, Li Y, *et al*. Low concentration isopropanol gas sensing properties of Ag nanoparticles decorated In_2O_3 hollow spheres. *J Adv Ceram* 2022, **11**: 379–391.
[9] Xu JY, Zhang C. Oxygen vacancy engineering on cerium oxide nanowires for room-temperature linalool detection in rice aging. *J Adv Ceram* 2022, **11**: 1559–1570.
[10] Zhao SK, Shen YB, Yan XX, *et al*. Complex-surfactant-assisted hydrothermal synthesis of one-dimensional ZnO nanorods for high-performance ethanol gas sensor. *Sensor Actuat B-Chem* 2019, **286**: 501–511.
[11] Renitta A, Vijayalakshmi K. A novel room temperature ethanol sensor based on catalytic Fe activated porous WO_3 microspheres. *Catal Commun* 2016, **73**: 58–62.
[12] Zhang MX, Liu K, Zhang XM, *et al*. Interfacial energy barrier tuning of hierarchical Bi_2O_3/WO_3 heterojunctions for advanced triethylamine sensor. *J Adv Ceram* 2022, **11**: 1860–1872.
[13] Liu D, Ren XW, Li YS, *et al*. Nanowires-assembled WO_3 nanomesh for fast detection of ppb-level NO_2 at low temperature. *J Adv Ceram* 2020, **9**: 17–26.

[14] Shanbhag MM, Shetti NP, Kalanur SS, *et al*. Hf-doped tungsten oxide nanorods as electrode materials for electrochemical detection of paracetamol and salbutamol. *ACS Appl Nano Mater* 2022, **5**: 1263–1275.

[15] Hao Q, Liu T, Liu JY, *et al*. Controllable synthesis and enhanced gas sensing properties of a single-crystalline WO_3–rGO porous nanocomposite. *RSC Adv* 2017, **7**: 14192–14199.

[16] Zhu YY, Blackman C, Zhou PF, *et al*. Facile synthesis of Ag nanoparticles-decorated WO_3 nanorods and their application in O_2 sensing. *J Alloys Compd* 2023, **936**: 167930.

[17] Sun CX, Shao JK, Wang ZY, *et al*. CuO-sensitized amorphous $ZnSnO_3$ hollow-rounded cubes for highly sensitive and selective H_2S gas sensors. *Sensor Actuat B-Chem* 2022, **362**: 131799.

[18] Wattanawikkam C, Bootchanont A, Porjai P, *et al*. Phase evolution in annealed Ni-doped WO_3 nanorod films prepared via a glancing angle deposition technique for enhanced photoelectrochemical performance. *Appl Surf Sci* 2022, **584**: 152581.

[19] Zhang Y, Han S, Wang MY, *et al*. Electrospun Cu-doped In_2O_3 hollow nanofibers with enhanced H_2S gas sensing performance. *J Adv Ceram* 2022, **11**: 427–442.

[20] Ciciliati MA, Silva MF, Fernandes DM, *et al*. Fe-doped ZnO nanoparticles: Synthesis by a modified sol–gel method and characterization. *Mater Lett* 2015, **159**: 84–86.

[21] John RAB, Ruban Kumar A, Shruthi J, *et al*. $Fe_xZn_{1-x}O_y$ as room temperature dual sensor for formaldehyde and ammonia gas detection. *Inorg Chem Commun* 2022, **141**: 109506.

[22] Zheng ZC, Liu KW, Xu KC, *et al*. Investigation on microstructure and nonanal sensing properties of hierarchical Sb_2WO_6 microspheres. *Ceram Int* 2022, **48**: 30249–30259.

[23] Liu KW, Zheng ZC, Xu JY, *et al*. Enhanced visible light-excited $ZnSnO_3$ for room temperature ppm-level CO_2 detection. *J Alloys Compd* 2022, **907**: 164440.

[24] Barsan N, Schweizer-Berberich M, Göpel W. Fundamental and practical aspects in the design of nanoscaled SnO_2 gas sensors: A status report. *Fresen J Anal Chem* 1999, **365**: 287–304.

[25] Meng SG, Li DZ, Fu XL, *et al*. Integrating photonic bandgaps with surface plasmon resonance for the enhancement of visible-light photocatalytic performance. *J Mater Chem A* 2015, **3**: 23501–23511.

[26] Shannon RD. Revised effective ionic radii and systematic studies of interatomic distances in halides and chalcogenides. *Acta Crystallogr A* 1976, **32**: 751–767.

[27] Wu JX, Zou S, Wang B, *et al*. Enhanced acetone sensing properties of W-doped $ZnFe_2O_4$ electrospinning nanofibers. *J Alloys Compd* 2023, **938**: 168440.

[28] Gu JQ, Zhang B, Li YW, *et al*. Synthesis of spindle-like Co-doped $LaFeO_3$ porous microstructure for high performance n-butanol sensor. *Sensor Actuat B-Chem* 2021, **343**: 130125.

[29] Zhang YQ, Wang C, Zhao LJ, *et al*. Preparation of Ce-doped SnO_2 cuboids with enhanced 2-butanone sensing performance. *Sensor Actuat B-Chem* 2021, **341**: 130039.

[30] Turgut G, Sonmez E, Aydın S, *et al*. The effect of Mo and F double doping on structural, morphological, electrical and optical properties of spray deposited SnO_2 thin films. *Ceram Int* 2014, **40**: 12891–12898.

[31] Du WJ, Si WX, Wang FL, *et al*. Creating oxygen vacancies on porous indium oxide nanospheres via metallic aluminum reduction for enhanced nitrogen dioxide detection at low temperature. *Sensor Actuat B-Chem* 2020, **303**: 127221.

[32] Huang JY, Jiang DT, Zhou JX, *et al*. Visible light-activated room temperature NH_3 sensor base on CuPc-loaded ZnO nanorods. *Sensor Actuat B-Chem* 2021, **327**: 128911.

[33] Geng X, Li SW, Mawella-Vithanage L, *et al*. Atomically dispersed Pb ionic sites in PbCdSe quantum dot gels enhance room-temperature NO_2 sensing. *Nat Commun* 2021, **12**: 4895.

[34] Bittencourt C, Landers R, Llobet E, *et al*. The role of oxygen partial pressure and annealing temperature on the formation of W=O bonds in thin WO_3 films. *Semicond Sci Technol* 2002, **17**: 522–525.

[35] Rougier A, Portemer F, Quédé A, *et al*. Characterization of pulsed laser deposited WO_3 thin films for electrochromic devices. *Appl Surf Sci* 1999, **153**: 1–9.

[36] Xin X, Lang JY, Wang TT, *et al*. Construction of novel ternary component photocatalyst $Sr_{0.25}H_{1.5}Ta_2O_6{\cdot}H_2O$ coupled with g-C_3N_4 and Ag toward efficient visible light photocatalytic activity for environmental remediation. *Appl Catal B* 2016, **181**: 197–209.

[37] Du WJ, Si WX, Zhao JB, *et al*. Mesoporous Fe-doped In_2O_3 nanorods derived from metal organic frameworks for enhanced nitrogen dioxide detection at low temperature. *Ceram Int* 2020, **46**: 20385–20394.

[38] Li PP, Cao CY, Shen QK, *et al*. Cr-doped NiO nanoparticles as selective and stable gas sensor for ppb-level detection of benzyl mercaptan. *Sensor Actuat B-Chem* 2021, **339**: 129886.

[39] Valero-Romero MJ, Santaclara JG, Oar-Arteta L, *et al*. Photocatalytic properties of TiO_2 and Fe-doped TiO_2 prepared by metal organic framework-mediated synthesis. *Chem Eng J* 2019, **360**: 75–88.

[40] Li JJ, Zhang M, Weng B, *et al*. Oxygen vacancies mediated charge separation and collection in Pt/WO_3 nanosheets for enhanced photocatalytic performance. *Appl Surf Sci* 2020, **507**: 145133.

[41] Pan XY, Yang MQ, Fu XZ, *et al*. Defective TiO_2 with oxygen vacancies: Synthesis, properties and photocatalytic applications. *Nanoscale* 2013, **5**: 3601–3614.

[42] Wang Y, Cui YY, Meng XN, *et al*. A gas sensor based on Ag-modified ZnO flower-like microspheres: Temperature-modulated dual selectivity to CO and CH_4. *Surf Interfaces* 2021, **24**: 101110.

[43] Nguyen JL, Dockery DW. Daily indoor-to-outdoor temperature and humidity relationships: A sample across

seasons and diverse climatic regions. *Int J Biometeorol* 2016, **60**: 221–229.

[44] Jafari N, Zeinali S, Shadmehr J. Room temperature resistive gas sensor based on ZIF-8/MWCNT/AgNPs nanocomposite for VOCs detection. *J Mater Sci-Mater El* 2019, **30**: 12339–12350.

[45] Zhao SK, Shen YB, Maboudian R, *et al*. Facile synthesis of ZnO–SnO_2 hetero-structured nanowires for high-performance NO_2 sensing application. *Sensor Actuat B-Chem* 2021, **333**: 129613.

[46] Wang ZH, Zhi MF, Xu MZ, *et al*. Ultrasensitive NO_2 gas sensor based on Sb-doped SnO_2 covered ZnO nano-heterojunction. *J Mater Sci* 2021, **56**: 7348–7356.

[47] Li XB, Kang BB, Dong F, *et al*. Enhanced photocatalytic degradation and H_2/H_2O_2 production performance of S–pCN/$WO_{2.72}$ S-scheme heterojunction with appropriate surface oxygen vacancies. *Nano Energy* 2021, **81**: 105671.

[48] Wang JP, Wang ZY, Huang BB, *et al*. Oxygen vacancy induced band-gap narrowing and enhanced visible light photocatalytic activity of ZnO. *ACS Appl Mater Interfaces* 2012, **4**: 4024–4030.

[49] Li JH, Wu J, Yu YX. DFT exploration of sensor performances of two-dimensional WO_3 to ten small gases in terms of work function and band gap changes and *I–V* responses. *Appl Surf Sci* 2021, **546**: 149104.

[50] Geng X, Liu XL, Mawella-Vithanage L, *et al*. Photoexcited NO_2 enables accelerated response and recovery kinetics in light-activated NO_2 gas sensing. *ACS Sens* 2021, **6**: 4389–4397.

[51] Ma Z, Chen P, Cheng W, *et al*. Highly sensitive, printable nanostructured conductive polymer wireless sensor for food spoilage detection. *Nano Lett* 2018, **18**: 4570–4575.

Open Access This article is licensed under a Creative Commons Attribution 4.0 International License, which permits use, sharing, adaptation, distribution and reproduction in any medium or format, as long as you give appropriate credit to the original author(s) and the source, provide a link to the Creative Commons licence, and indicate if changes were made.

The images or other third party material in this article are included in the article's Creative Commons licence, unless indicated otherwise in a credit line to the material. If material is not included in the article's Creative Commons licence and your intended use is not permitted by statutory regulation or exceeds the permitted use, you will need to obtain permission directly from the copyright holder.

To view a copy of this licence, visit http://creativecommons.org/licenses/by/4.0/.